

Lawrence Berkeley National Laboratory

LBL Publications

Title

Determination of the structural phase and octahedral rotation angle in halide perovskites

Permalink

<https://escholarship.org/uc/item/99540471>

Journal

Applied Physics Letters, 112(7)

ISSN

0003-6951

Authors

dos Reis, Roberto
Yang, Hao
Ophus, Colin
[et al.](#)

Publication Date

2018-02-12

DOI

10.1063/1.5017537

Peer reviewed

Determination of the structural phase and octahedral rotation angle in halide perovskites

Roberto dos Reis, Hao Yang, Colin Ophus, Peter Ercius, Gregory Bizarri, Didier Perrodin, Tetiana Shalapska, Edith Bourret, Jim Ciston, and Ulrich Dahmen

Citation: *Appl. Phys. Lett.* **112**, 071901 (2018); doi: 10.1063/1.5017537

View online: <https://doi.org/10.1063/1.5017537>

View Table of Contents: <http://aip.scitation.org/toc/apl/112/7>

Published by the [American Institute of Physics](#)

Articles you may be interested in

[Exciton-phonon coupling in a CsPbBr₃ single nanocrystal](#)

Applied Physics Letters **112**, 072104 (2018); 10.1063/1.5018413

[Efficient CH₃NH₃PbI₃ perovskite/fullerene planar heterojunction hybrid solar cells with oxidized Ni/Au/Cu transparent electrode](#)

Applied Physics Letters **112**, 071103 (2018); 10.1063/1.5006513

[Excitonic nature of optical transitions in electroabsorption spectra of perovskite solar cells](#)

Applied Physics Letters **112**, 083902 (2018); 10.1063/1.5017943

[Creation and annealing of metastable defect states in CH₃NH₃PbI₃ at low temperatures](#)

Applied Physics Letters **112**, 081102 (2018); 10.1063/1.5019921

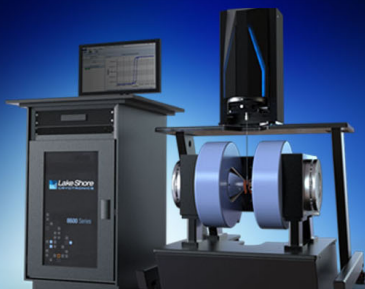
[Micropillars with a controlled number of site-controlled quantum dots](#)

Applied Physics Letters **112**, 071101 (2018); 10.1063/1.5017692

[Interface engineering of CsPbBr₃/TiO₂ heterostructure with enhanced optoelectronic properties for all-inorganic perovskite solar cells](#)


Applied Physics Letters **112**, 093901 (2018); 10.1063/1.5019608

 **Lake Shore**
CRYOTRONICS



NEW 8600 Series VSM

For fast, highly sensitive
measurement performance

LEARN MORE 

Determination of the structural phase and octahedral rotation angle in halide perovskites

Roberto dos Reis,^{1,a)} Hao Yang,^{1,b)} Colin Ophus,¹ Peter Ercius,¹ Gregory Bizarri,² Didier Perrodin,² Tetiana Shalapska,² Edith Bourret,² Jim Ciston,^{1,c)} and Ulrich Dahmen¹

¹National Center for Electron Microscopy, Molecular Foundry, Lawrence Berkeley National Laboratory, Berkeley, California 94720, USA

²Materials Sciences Division, Lawrence Berkeley National Laboratory, Berkeley, California 94720, USA

(Received 28 November 2017; accepted 9 January 2018; published online 12 February 2018)

A key to the unique combination of electronic and optical properties in halide perovskite materials lies in their rich structural complexity. However, their radiation sensitive nature limits nanoscale structural characterization requiring dose efficient microscopic techniques in order to determine their structures precisely. In this work, we determine the space-group and directly image the Br halide sites of CsPbBr₃, a promising material for optoelectronic applications. Based on the symmetry of high-order Laue zone reflections of convergent-beam electron diffraction, we identify the tetragonal (I4/mcm) structural phase of CsPbBr₃ at cryogenic temperature. Electron ptychography provides a highly sensitive phase contrast measurement of the halide positions under low electron-dose conditions, enabling imaging of the elongated Br sites originating from the *out-of-phase* octahedral rotation viewed along the [001] direction of I4/mcm persisting at room temperature. The measurement of these features and comparison with simulations yield an octahedral rotation angle of 6.5° (±1.5°). The approach demonstrated here opens up opportunities for understanding the atomic scale structural phenomena applying advanced characterization tools on a wide range of radiation sensitive halide-based all-inorganic and hybrid organic-inorganic perovskites. *Published by AIP Publishing.*

<https://doi.org/10.1063/1.5017537>

Recently, halide-based perovskites have drawn substantial interest as promising materials for high-efficiency solar energy harvesting due to their excellent optoelectronic properties, low-cost, and material accessibility.^{1–3} Various combinations of optical and electronic properties can be achieved by altering their structures,^{4–6} and a precise knowledge of the atomic configuration is vital for a complete understanding of the structure-property relationship. Particularly, development of Pb-halide structures, such as CsPbX₃, without a volatile organic compound, can provide a higher durability for photovoltaic cells.⁷ In addition, CsPbBr₃ presents better mechanical stability and optoelectronic properties for applications in X- and γ -ray radiation detectors.⁸

Initial studies on halide perovskites CsPbX₃ by Möller in the 1950s^{9,10} described the structure of CsPbBr₃ as a monoclinic distorted perovskite at room temperature. In single crystals, the low- and room-temperature phases have been reported to be orthorhombic^{8,11} evolving to tetragonal with increasing temperature and to cubic for temperatures above 130 °C. In nanostructures, the cubic structure¹² has been predominant.¹³ Recent first principles calculations¹⁴ have shown that octahedral units in halide perovskites generally prefer *in-phase* rotations,¹⁵ though a cubic-to-tetragonal (I4/mcm) transformation through *out-of phase* rotations¹⁵ has also been found.^{16,17} The typical yellow-orange color of CsPbBr₃ single crystals (Fig. S1 in the [supplementary material](#)) has been attributed to an orthorhombic phase with a bandgap of 2.25 eV.⁸ However, the challenge remains in determining the

symmetry and quantifying the octahedral rotations accurately as the crystal structural phase can vary with the size and growth technique.

Most of the structural characterization studies in halide perovskites have been performed using X-ray or neutron diffraction.^{8–12,16,17} Unfortunately, these techniques offer a limited spatial resolution and low sensitivity to small symmetry deviations, such as the absence of center of symmetry and effects due to small atomic shifts,¹⁸ hence presenting significant challenges to precisely distinguish the mesoscale structural complexity of different phases and octahedral tilting configurations. Advances in aberration corrected (scanning) transmission electron microscopy (S)TEM over the few past decades have significantly improved the accuracy of structure determination with a sub-Å resolution.^{19–22} However, it remains difficult to characterize halide perovskites due to their high sensitivity to electron radiation damages.²³ Recently, Yu *et al.*¹³ demonstrated that by reducing the electron dose, it is possible to achieve atomic resolution images of ultrathin CsPbBr₃ nanoplates using a phase contrast imaging technique named exit-wave reconstruction.

Here, we apply electron diffraction based techniques, including convergent beam electron diffraction (CBED) and electron ptychography, to unambiguously determine the space-group and estimate the octahedral rotations of the all-inorganic halide perovskite CsPbBr₃ under low dose conditions. CBED can uniquely determine space-group symmetries²⁴ at the scale of few nanometers enabling probing defect-free areas within the crystal and has been applied to many different materials over the past few decades.^{25–29} Space group symmetry elements such as screw axes, glide

^{a)}Electronic mail: rmsdosreis@lbl.gov.

^{b)}H. Yang contributed equally to this work.

^{c)}Electronic mail: jciston@lbl.gov.

planes, and non-centrosymmetric axes can be identified by observing the presence or absence of dynamical extinction lines due to dynamical scattering effects.^{30–32} Moreover, high order Laue-Zone (HOLZ) reflections in CBED are sensitive to the subtle displacements of atoms along the projected beam direction and can be used to identify the symmetry departures from its ideal structural phase.³³

For atomic resolution low dose imaging, we use electron ptychography, which is known for providing a quantitative measure of the phase changes of the incident coherent electron wave as it propagates through an electron transparent specimen.³⁴ This technique offers a highly efficient phase contrast transfer function and excellent image contrast of light elements under low dose imaging conditions.³⁵ Recent advances in the fast pixelated detector technology have allowed atomic resolution phase images to be achieved simultaneously using the incoherent Z-contrast imaging method in High-angle Annular Dark Field (HAADF) STEM,^{36,37} therefore providing great sensitivity for imaging both light and heavy elements.

Single crystals of CsPbBr₃, grown via the Bridgman-Stockbarger technique, were crushed to powder and dropped on ultrathin C-coated Cu grids. CBED experiments were performed using a Zeiss Libra MC200 operated at 200 kV. CBED patterns were collected using a convergence semi-angle of 1.6 mrad and recorded using a Gatan 894 Ultrascan with the sample kept at liquid nitrogen (LN) temperature (≈ 77 K). For reconstructions, the electron diffraction patterns at each probe position were recorded at room-temperature (≈ 300 K) using a Gatan K2 IS direct electron detector operated at 800 frames per second installed on TEAM I, an aberration-corrected FEI Titan 80–300 operated in the STEM mode at 300 kV with a convergence semi-angle of 17.2 mrad. The camera acquisition and probe scanning were synchronized using a Gatan Digiscan and STEMx software package. The simultaneous annular dark field (ADF) image was acquired with collection angles of 40–240 mrad. The probe was scanned over 256×256 probe positions to create a $256 \times 256 \times 1920 \times 895$ four-dimensional (4D) dataset, namely, 4D-STEM. Data post processing was performed using custom scripts written in MATLAB. Multislice simulations were performed using custom MATLAB codes that follow the methods of Kirkland³⁸ applying sixteen frozen phonon configurations. Simulated 4D-STEM datasets are composed of a mesh of 35×35 probe positions per unit cell with the FWHM of the probe set to 0.8 Å. The lattice parameter was initially set using the cubic structure reported by Stoumpos *et al.*⁸ and transformed to tetragonal by applying $a = \sqrt{2}a$, $b = \sqrt{2}a$, and $c = 2a$ expansion. To generate *out-of-phase* rotations, we applied a shift (δx) to the 8h Wyckoff position of the *I4/mcm* space group. The shift is related to the octahedral unit rotation angle by $\phi = \tan^{-1}(1 - 4x')$, where $x' = x + \delta x$ is the updated fractional coordinate for 8h. Ptychography reconstructions were applied to both experimental and simulated 4D datasets using the Wigner distribution deconvolution (WDD) method.³⁹

We can narrow the possible structures of CsPbBr₃ following the pathways of distortions from the ideal cubic structure [Fig. 1(a)] by applying the group-subgroup relationship (Fig. S2 in the [supplementary material](#)). *In-phase* or

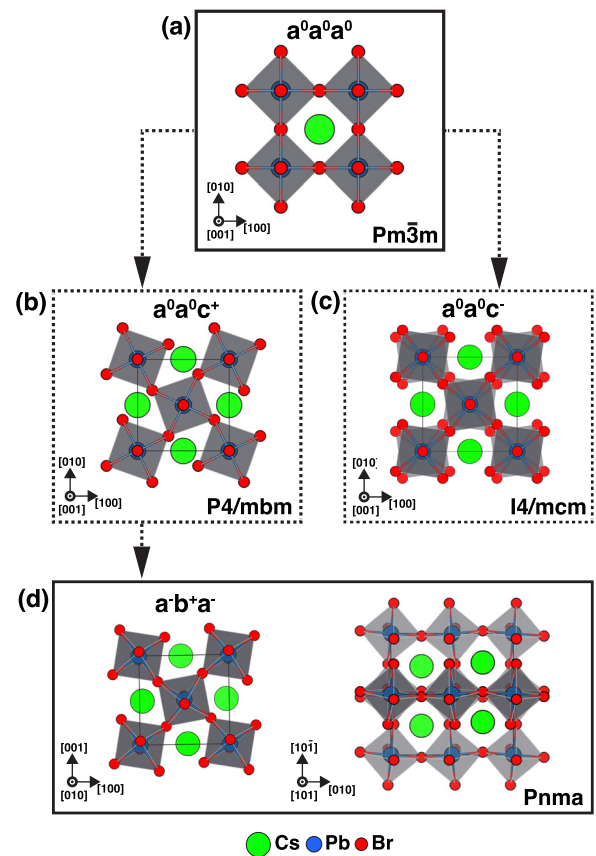


FIG. 1. Possible crystal structures of CsPbBr₃ following the group-subgroup relationship for perovskites. (a) Cubic *Pm* $\bar{3}$ *m*, the aristotype crystal, denoted by Glazer notation $a^0a^0a^0$. (b) Tetragonal phase *P4/mbm* generated by *in-phase* rotation *P4/mbm* denoted by $a^0a^0c^+$. (c) Tetragonal, *I4/mcm* generated by *out-of-phase* rotation, denoted by $a^0a^0c^-$. (d) *Pnma* structure viewed along *in-plane*, $[010]_O$, and out of plane $[101]_O$ of the pseudocubic axis of the orthorhombic structure.

out-of-phase octahedral unit rotation around the fourfold $[001]$ axis results in tetragonal *P4/mbm* [Fig. 1(b)] or *I4/mcm* [Fig. 1(c)] symmetries, respectively, with $a^0a^0c^+$ or $a^0a^0c^-$ Glazer tilt system notation. The symmetry can be lowered further to orthorhombic *Pnma* [Fig. 1(d)] through additional rotations along $[100]$ and $[010]$ axes ($a^-b^+a^-$).⁴⁰

In principle, the crystal symmetries presented in Fig. 1 can be fully distinguished by analyzing CBED patterns taken at one of the high symmetry pseudocubic projections⁴¹ perpendicular to the alternating layers where the displacements of Br take place during phase transformations. Figure 2(a) shows a representation of two-dimensional (2D) plane groups that can be used to unambiguously distinguish the possible space groups. For example, along $[001]$, space groups *Pm* $\bar{3}$ *m* and *I4/mcm* have a 2D projected symmetry **p4mm**, and *P4/mbm* has a 2D projected symmetry **p4gm**. Pseudocubic axes of the orthorhombic *Pnma* structure were $[010]_O$ and $[101]_O$ with projected symmetries **p2gg** and **p2mm**, respectively. Figure 2(b) presents a zero-order Laue zone (ZOLZ)-CBED pattern taken at the pseudocubic $[001]_{pc}$ axis, alongside a simulated ZOLZ-CBED pattern assuming a cubic *Pm* $\bar{3}$ *m* crystal. The patterns clearly show the presence of mirror planes indicated by the arrowheads *m1* and *m2*, depicting a **p4mm** plane group. The observed projected symmetry in the ZOLZ-CBED rules out the orthorhombic *Pnma* crystal system.

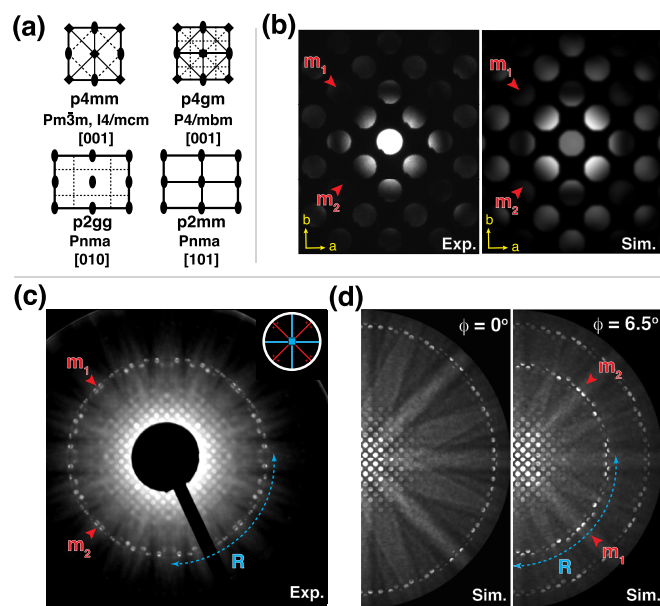


FIG. 2. (a) 2-D representation of possible plane symmetries for $CsPbBr_3$. (b) Experimental CBED pattern along [001] acquired at LN temperature showing a $4mm$ symmetry, indicated by the arrowheads m_1 and m_2 alongside the simulated pattern for a cubic $Pm\bar{3}m$ with a thickness of $600(\pm 10)$ Å. (c) Experimental high order Laue zone pattern acquired at LN temperature exhibiting a fourfold rotation and two mirror symmetries, with an overall symmetry of $p4mm$. The inset shows the geometrical representation for a $p4mm$ symmetry. (d) Simulated CBED for cubic $Pm\bar{3}m$ ($\phi = 0^\circ$) and tetragonal $I4/m\bar{c}m$ ($\phi = 6.5^\circ$) along [001]. Arrowheads m_1 and m_2 highlight the two mirror symmetries and the dotted arc indicates a fourfold rotation.

Figure 2(c) shows HOLZ reflections at the same crystal orientation as in Fig. 2(b). HOLZ diffraction probes the subtle symmetry distortions along the beam direction distinguishing between the projected symmetries of possible tetragonal $I4/m\bar{c}m$ and $P4/mbm$ along the [001] direction (same as $[001]_{pc}$) and $Pm\bar{3}m$. The pattern clearly exhibits a fourfold rotation symmetry indicated by a dotted arc, and two mirror symmetries indicated by the arrowheads m_1 and m_2 , with a total projected symmetry of $p4mm$. This symmetry reduction takes place through displacements of Br sites at Wyckoff position 8h, which possess an $m2m$ point symmetry. These *out-of-phase* displacements result in a superlattice reflection where Br sites contribute to the hkl ($h, k = \text{even}$) first-order Laue zone (FOLZ) reflections. Figure 2(d) shows HOLZ pattern simulations for $Pm\bar{3}m$ and $I4/m\bar{c}m$ along the [001] axis for a thickness of 600 Å and lattice parameters $a = b = 7.7$ Å and $c = 13.5$ Å. To generate the break of symmetry along the beam direction leading to the $I4/m\bar{c}m$ space group, a shift $\delta x = 0.195$ in fractional coordinate units was applied to Br atoms at 8h sites (see Fig. S3 in the [supplementary material](#) for simulations applying different rotations and thicknesses). Such displacement corresponds to a $PbBr_6$ octahedral rotation angle (ϕ) of $\approx 6.5^\circ$. The appearance of superlattice FOLZ reflection possessing a $p4mm$ symmetry in the simulated CBED clearly matches the symmetry of the experimental pattern. The Br shift applied in Fig. 2(d) was chosen based on the estimation of the octahedral angle shown in the following ptychographic measurements. It is important to notice that any break of symmetry along the Z axis would produce an extra HOLZ line (see Fig. S3 in the [supplementary material](#)). Further structure refinement based on the FOLZ and SOLZ

relative intensity is possible in order to determine the rotation angle values as shown by Tsuda and Tanaka.³³

Electron ptychography was applied for direct imaging Br sites and displacements due to the *out-of-phase* octahedral rotations enforced by the $I4/m\bar{c}m$ symmetry established by CBED. The 4D datasets acquired at room temperature using a fast pixelated direct electron detector contain redundant phase information that can be extracted using electron ptychography.³⁷ The relatively total low electron dose applied in this work ($\approx 10^3 e \text{ \AA}^{-2}$) reduces the specimen damage by the electron radiation. Before and after images confirm that the specimen remained undamaged after recording the ptychographic dataset (see Fig. S4 in the [supplementary material](#)). As individual diffraction patterns recorded with a short dwell time of 1.3 ms have a poor signal-to-noise ratio, the diffraction patterns were denoised using a clusterization procedure⁴² prior to applying ptychographic reconstruction improving the signal to noise of individual diffraction patterns (see Fig. S5 in the [supplementary material](#)).

Figure 3(a) shows an incoherent Z-contrast image recorded simultaneously with the ptychographic dataset using an annular dark field (ADF) detector. The inset shows a unit cell average of the experimental image. The ADF image provides a good contrast for Cs and Pb sites; however, Br visibility is much lower due to the low signal-to-noise

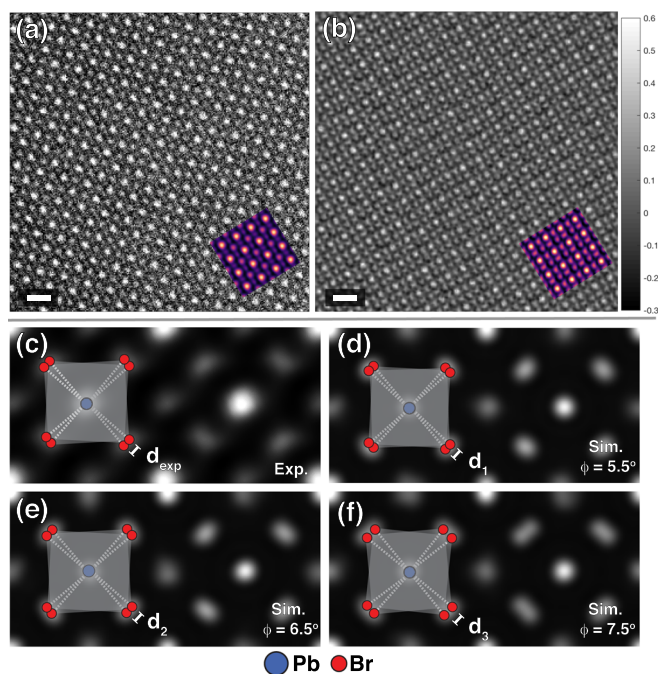


FIG. 3. (a) Simultaneously acquired ADF image showing high contrast for Cs and Pb sites, with poor Br contrast. (b) Ptychographically reconstructed phase image from the 4D-STEM dataset shows an improved contrast for all elements with projected vertical and horizontal stretches of Br sites. The insets in (a) and (b) show an averaged unit cell of the experimental images. The scale bar is 5 Å, and the color bar in (b) is in units of radian. (c) Experimental reconstructed phase image [same as the inset in (b)] compared with three different phase images reconstructed from a 4D-STEM simulated dataset corresponding, respectively, to octahedral rotations of (d) 5.5° , (e) 6.5° , and (f) 7.5° . A specimen thickness of 200 Å was used in the simulations. The experimental distance $d_{exp} = 0.57$ Å matches the d_2 value measured from simulated ptychographic reconstruction in e. The values of d_{exp} , d_1 , d_2 , and d_3 were quantified by fitting two 2D Gaussian peaks to the elongated Br columns corresponding to a projected $I4/m\bar{c}m$ structure along [001] axis as measured by CBED. All data acquired at 300 K.

ratio when imaged under low dose conditions. Figure 3(b) shows the phase of the ptychographically reconstructed complex specimen function, with a unit cell average shown as the inset. The phase image improves the contrast for all three elements including Br. In particular, fine details of the vertical and horizontal projected stretch of the Br are now visible in the phase image. The elongated Br columns are associated with the *out*-phase PbBr_6 octahedral unit rotation that leads to a small splitting of the Br columns when projected along the [001] axis of the $I4/mcm$ structure [Fig. 1(c)] determined by CBED (Fig. 2).

Comparison between experiment and a series of phase images ptychographically reconstructed from a 4D-STEM simulated dataset for different degrees of rotation allows us to estimate the experimental PbBr_6 octahedral rotation (see Fig. S6 in the [supplementary material](#)). To estimate the projected distance of the split Br columns, we assumed the presence of two overlapped peaks within the elongated sites—as in the $I4/mcm$ spacegroup viewed along the [001] axis—and refined the initial Br positions with nonlinear least squares two-dimensional Gaussian fitting (see Fig. S7 in the [supplementary material](#)). The experimental distance d_{exp} value of $0.57 \text{ \AA} \pm 0.18 \text{ \AA}$ was determined [Fig. 3(c)], with the uncertainty given by σ/\sqrt{N} of the applied metric (see details in the [supplementary material](#)). Figures 3(d), 3(e), and 3(f) show the results of ptychographically reconstructed phase images for simulated 4D-STEM datasets of structures with octahedral rotations of 5.5° , 6.5° , and 7.5° and the measured values $d_1 = 0.43 \text{ \AA}$, $d_2 = 0.58 \text{ \AA}$, and $d_3 = 0.74 \text{ \AA}$, respectively, from the same double Gaussian fit procedure. The d_{exp} value is most consistent with a 6.5° octahedral rotation, matching a direct geometric conversion of apparent Br sites in the phase reconstruction and implying a high degree of direct interpretability of the ptychography reconstruction even for thick specimens. The robustness of the reconstruction method for relatively thick foils, like the case presented here, is demonstrated in Fig. S8 in the [supplementary material](#) by determining the distance of the two Br related features in the phase reconstruction as a function of thickness (up to 400 \AA) and octahedral rotation angle, further supporting the angular error bar of 1.5° .

We have determined the structural phase and estimated the octahedral rotation of a CsPbBr_3 crystal under low dose conditions using a combination of CBED and electron ptychography. The presence of extra HOLZ reflections in the CBED patterns taken at LN temperature unambiguously assigns a $\mathbf{p4mm}$ symmetry with *out*-of-phase PbBr_6 octahedral unit rotations, which corresponds to the $I4/mcm$ tetragonal space group. This phase may be originated from the single crystal growth method applied in this work, and the precise control of the crystalline phase by varying growth parameters remains interesting to explore in the future. The ptychographic phase image provided a sensitive phase contrast of elongated Br columns owing to the *out*-of-phase octahedral rotation and enables further quantification of the projected distance of Br sites ($0.57 \pm 0.18 \text{ \AA}$) along the [001] axis of the $I4/mcm$ structure that corresponds to a rotation angle of $6.5^\circ \pm 1.5^\circ$ at room temperature in comparison to ptychographic reconstructions of fully dynamical scanning diffraction simulations. It is important to emphasize that the

transformation of tetragonal $I4/mcm$ to orthorhombic Pmna is forbidden and that CsPbBr_3 does not present structural changes until reaching 130°C . Therefore, the CBED result obtained at cryogenic temperature and ptychographic result at room temperature ensure that the $I4/mcm$ phase remains up to the point where CsPbBr_3 transforms to cubic. Also, based on the structural transformation of similar perovskite materials,¹⁶ we can infer that the octahedral rotation degree reduces as the temperature increases. In conclusion, we believe that our work demonstrates a powerful characterization routine that can be applied to studying a wide range of halide-based all-inorganic and inorganic-organic hybrid perovskites. Moreover, it opens up the opportunity to directly determine micro- and nano-scale structural mosaicism for a plethora of possible octahedral rotations, deformations, and off-centering in halide-based perovskites.

See [supplementary material](#) for photographs of a large single crystal of CsPbBr_3 analyzed in this work; group-subgroup relationship scheme among Glazer tilt systems highlighting possible phase transitions for CsPbBr_3 ; CBED simulations showing HOLZ reflections for different octahedral rotation angles and thicknesses; HAADF images acquired before, during, and after the acquisition of diffraction datasets with their corresponding fast-Fourier transformation (FFT); single diffraction and mean diffraction over the whole dataset with and without clusterization; panel of simulated ptychographic reconstructed phase images for different octahedral rotation angles and specimen thicknesses; double Gaussian fitting of the projected Br-Br bond length and related errors; and measured Br-Br projected bond length values as a function of the octahedral rotation angles for different simulated thicknesses.

The work at the Molecular Foundry was supported by the Office of Science, Office of Basic Energy Sciences, of the U.S. Department of Energy under Contract No. DE-AC02-05CH11231. D.P., T.S., G.B. and E.B. thank the support of the U.S. Department of Homeland Security/DNDO Contract No. DE-AC02-05CH11231. R.dR. and J.C. acknowledge support from the U.S. Department of Energy Early Career Research Program. R.dR. thanks Dr. Karen Bustillo for her help with experiments performed in the Libra microscope.

¹H. J. Snaith, *J. Phys. Chem. Lett.* **4**(21), 3623–3630 (2013).

²M. A. Green, A. Ho-Baillie, and H. J. Snaith, *Nat. Photonics* **8**(7), 506–514 (2014).

³M. Grätzel, *Nat. Mater.* **13**(9), 838–842 (2014).

⁴W.-J. Yin, T. Shi, and Y. Yan, *Adv. Mater.* **26**(27), 4653–4658 (2014).

⁵J. S. Manser, J. A. Christians, and P. V. Kamat, *Chem. Rev.* **116**(21), 12956–13008 (2016).

⁶M. R. Filip, G. E. Eperon, H. J. Snaith, and F. Giustino, *Nat. Commun.* **5**, 5757 (2014).

⁷J. Liang, C. Wang, Y. Wang, Z. Xu, Z. Lu, Y. Ma, H. Zhu, Y. Hu, C. Xiao, X. Yi *et al.*, *J. Am. Chem. Soc.* **138**(49), 15829–15832 (2016).

⁸C. C. Stoumpos, C. D. Malliakas, J. A. Peters, Z. Liu, M. Sebastian, J. Im, T. C. Chasapis, A. C. Wibowo, D. Y. Chung, A. J. Freeman, and B. W. Wessels, *Cryst. Growth Des.* **13**(7), 2722–2727 (2013).

⁹C. K. Møller, *Nature* **180**(4593), 981–982 (1957).

¹⁰C. K. Møller, *Nature* **182**(4647), 1436–1436 (1958).

¹¹M. Rodová, J. Brožek, K. Knížek, and K. Nitsch, *J. Therm. Anal. Calorim.* **71**(2), 667–673 (2003).

¹²L. Protesescu, S. Yakunin, M. I. Bodnarchuk, F. Krieg, R. Caputo, C. H. Hendon, R. X. Yang, A. Walsh, and M. V. Kovalenko, *Nano Lett.* **15**(6), 3692–3696 (2015).

- ¹³Y. Yu, D. Zhang, C. Kisielowski, L. Dou, N. Kornienko, Y. Bekenstein, A. B. Wong, A. P. Alivisatos, and P. Yang, *Nano Lett.* **16**(12), 7530–7535 (2016).
- ¹⁴J. Young and J. M. Rondinelli, *J. Phys. Chem. Lett.* **7**(5), 918–922 (2016).
- ¹⁵A. M. Glazer, *Acta Crystallogr. B* **28**(11), 3384–3392 (1972).
- ¹⁶Y. Kawamura, H. Mashiyama, and K. Hasebe, *J. Phys. Soc. Jpn.* **71**(7), 1694–1697 (2002).
- ¹⁷T. Baikie, N. S. Barrow, Y. Fang, P. J. Keenan, P. R. Slater, R. O. Piltz, M. Gutmann, S. G. Mhaisalkar, and T. J. White, *J. Mater. Chem. A* **3**(17), 9298–9307 (2015).
- ¹⁸J. M. Zuo, *Rep. Prog. Phys.* **67**(11), 2053 (2004).
- ¹⁹U. Dahmen, R. Erni, V. Radmilovic, C. Kisielowski, M.-D. Rossell, and P. Denes, *Philos. Trans. R. Soc. A* **367**(1903), 3795–3808 (2009).
- ²⁰R. Erni, M.-D. Rossell, C. Kisielowski, and U. Dahmen, *Phys. Rev. Lett.* **102**(9), 096101 (2009).
- ²¹P. E. Batson, N. Dellby, and O. L. Krivanek, *Nature* **418**(6898), 617–620 (2002).
- ²²P. D. Nellist, M. F. Chisholm, N. Dellby, O. L. Krivanek, M. F. Murfitt, Z. S. Szilagy, A. R. Lupini, A. Borisevich, W. H. Sides, and S. J. Pennycook, *Science* **305**(5691), 1741–1741 (2004).
- ²³Z. Dang, J. Shamsi, F. Palazon, M. Imran, Q. A. Akkerman, S. Park, G. Bertoni, M. Prato, R. Brescia, and L. Manna, *ACS Nano* **11**(2), 2124–2132 (2017).
- ²⁴B. F. Buxton, J. Eades, J. T. Steeds, and G. M. Rackham, *Philos. Trans. R. Soc. A* **281**(1301), 171–194 (1976).
- ²⁵M. Tanaka, *Acta Crystallogr. A* **50**(3), 261–286 (1994).
- ²⁶M. Tanaka and K. Tsuda, *J. Electron Microsc.* **60**(suppl 1), S245–S267 (2011).
- ²⁷J. M. Zuo and J. C. H. Spence, *Advanced Transmission Electron Microscopy: Imaging and Diffraction in Nanoscience* (Springer, 2016).
- ²⁸J. C. H. Spence, *Acta Crystallogr. A* **49**(2), 231–260 (1993).
- ²⁹K.-H. Kim, D. A. Payne, and J. M. Zuo, *Appl. Phys. Lett.* **107**(16), 162902 (2015).
- ³⁰J. Gjønnes and A. F. Moodie, *Acta Crystallogr.* **19**(1), 65–67 (1965).
- ³¹M. Tanaka, H. Sekii, and T. Nagasawa, *Acta Crystallogr. A* **39**(6), 825–837 (1983).
- ³²Z. Liliental-Weber and L. Parechianian-Allen, *Appl. Phys. Lett.* **49**(18), 1190–1192 (1986).
- ³³K. Tsuda and M. Tanaka, *Acta Crystallogr. A* **51**(1), 7–19 (1995).
- ³⁴J. M. Rodenburg, *Adv. Imaging Electron Phys.* **150**, 87–184 (2008).
- ³⁵H. Yang, T. J. Pennycook, and P. D. Nellist, *Ultramicroscopy* **151**, 232–239 (2015).
- ³⁶T. J. Pennycook, A. R. Lupini, H. Yang, M. F. Murfitt, L. Jones, and P. D. Nellist, *Ultramicroscopy* **151**, 160–167 (2015).
- ³⁷H. Yang, R. N. Rutte, L. Jones, M. Simson, R. Sagawa, H. Ryll, M. Huth, T. J. Pennycook, M. L. H. Green, H. Soltau *et al.*, *Nat. Commun.* **7**, 12532 (2016).
- ³⁸E. J. Kirkland, *Advanced Computing in Electron Microscopy* (Springer, 2010).
- ³⁹J. M. Rodenburg and R. H. T. Bates, *Philos. Trans. R. Soc. A* **339**(1655), 521–553 (1992).
- ⁴⁰C. J. Howard and H. T. Stokes, *Acta Crystallogr. B* **54**(6), 782–789 (1998).
- ⁴¹J. W. Steeds and R. Vincent, *J. Appl. Cryst.* **16**(3), 317–324 (1983).
- ⁴²M. Battaglia, D. Contarato, P. Denes, and P. Giubilato, *Nucl. Instrum. Methods Phys. Res. A* **608**(2), 363–365 (2009).